

A fast-response self-powered UV-Vis-NIR broadband photodetector based on a $AgIn_5Se_8$/t-Se heterojunction

Kang Li(李康), Lei Xu(许磊), Qidong Lu(陆启东), and Peng Hu(胡鹏)
Citation: Chin. Phys. B, 2023, 32 (**11**): 118503. DOI: 10.1088/1674-1056/acec44
Journal homepage: http://cpb.iphy.ac.cn; http://iopscience.iop.org/cpb

What follows is a list of articles you may be interested in

Investigation of Ga_2O_3/diamond heterostructure solar-blind avalanche photodiode via TCAD simulation

Dun-Zhou Xu(许敦洲), Peng Jin(金鹏), Peng-Fei Xu(徐鹏飞), Meng-Yang Feng(冯梦阳), Ju Wu(吴巨), and Zhan-Guo Wang(王占国)
Chin. Phys. B, 2023, 32 (**10**): 108504. DOI: 10.1088/1674-1056/acc44d

Novel layout design of 4H-SiC merged PiN Schottky diodes leading to improved surge robustness

Jia-Hao Chen(陈嘉豪), Ying Wang(王颖), Xin-Xing Fei(费新星), Meng-Tian Bao(包梦恬), and Fei Cao(曹菲)
Chin. Phys. B, 2023, 32 (**9**): 098505. DOI: 10.1088/1674-1056/acad6b

A SiC asymmetric cell trench MOSFET with a split gate and integrated p^+-poly Si/SiC heterojunction freewheeling diode

Kaizhe Jiang(蒋铠哲), Xiaodong Zhang(张孝冬), Chuan Tian(田川), Shengrong Zhang(张升荣),Liqiang Zheng(郑理强), Rongzhao He(赫荣钊), and Chong Shen(沈重)
Chin. Phys. B, 2023, 32 (**5**): 058504. DOI: 10.1088/1674-1056/acbd2d

Low switching loss and increased short-circuit capability split-gate SiC trench MOSFET with p-type pillar

Pei Shen(沈培), Ying Wang(王颖), Xing-Ji Li(李兴冀), Jian-Qun Yang(杨剑群), and Fei Cao(曹菲)
Chin. Phys. B, 2023, 32 (**5**): 058501. DOI: 10.1088/1674-1056/ac98a1

Dynamic modeling of total ionizing dose-induced threshold voltage shifts in MOS devices

Guangbao Lu(陆广宝), Jun Liu(刘俊), Chuanguo Zhang(张传国), Yang Gao(高扬), and Yonggang Li(李永钢)
Chin. Phys. B, 2023, 32 (**1**): 018506. DOI: 10.1088/1674-1056/ac9fc4

SPECIAL TOPIC — Celebrating the 100th Anniversary of Physics Discipline of Northwest University

A fast-response self-powered UV–Vis–NIR broadband photodetector based on a $AgIn_5Se_8$/t-Se heterojunction

Kang Li(李康), Lei Xu(许磊), Qidong Lu(陆启东), and Peng Hu(胡鹏)[†]

School of Physics, Northwest University, Xi'an 710127, *China*

(Received 14 June 2023; revised manuscript received 25 July 2023; accepted manuscript online 1 August 2023)

A type II p–n heterojunction could improve the photodetection performance of a photodetector due to the excellent ability of carrier separation. N-type $AgIn_5Se_8$ (AIS) exhibits a large optical absorption coefficient, high optical conductivity and a suitable bandgap, and shows potential application in broadband photodetection. Even though our previous study on $AgIn_5Se_8$/$FePSe_3$ obtained a good response speed, it still gave low responsivity due to the poor quality of the p-type $FePSe_3$ thin film. Se, with a direct bandgap (around 1.7 eV), p-type conductivity, high electron mobility and high carrier density, is likely to form a low-dimensional structure, which leads to an increase in the effective contact area of the heterojunction and further improves the photodetector performance. In this work, continuous and dense t-Se thin film was prepared by electrochemical deposition. The self-powered $AgIn_5Se_8$/t-Se heterojunction photodetector exhibited a broadband detection range from 365 nm to 1200 nm. The responsivity and detectivity of the heterojunction photodetector were 32 μA/W and 1.8×10^9 Jones, respectively, which are around 9 and 4 times higher than those of the $AgIn_5Se_8$/$FePSe_3$ heterojunction photodetector. The main reason for this is the good quality of the t-Se thin film and the formation of the low-dimensional t-Se nanoribbons, which optimized the transport pathway of carriers. The results indicate that the $AgIn_5Se_8$/t-Se heterojunction is an excellent candidate for broadband and self-powered photoelectronic devices.

Keywords: $AgIn_5Se_8$/t-Se heterojunction, self-power broadband photodetector

PACS: 85.30.–z, 85.60.Gz, 73.61.Le **DOI:** 10.1088/1674-1056/acec44

1. Introduction

Based on the photoelectric effect, a photodetector, an electromagnetic detection energy sensor, converts optical signals into electrical signals, and has a wide range of applications in the industry and military fields,[1–7] such as missile guidance and infrared imaging.[8–10] Conventional photodetectors generally require a bias voltage, which results in the expansion and complexity of the photoelectrical device and also limits application in some special environments.[9,11] Furthermore, broadband detection (UV–Vis–NIR) is an effective way to minimize the volume of the photodetection system.[6,12–17] Therefore, self-powered broadband photodetectors are becoming an important development direction for future photodetectors. One way to achieve the self-powered photoresponse is to construct heterojunctions,[18–21] which lead to the rapid separation of the photogenerated electron–hole pairs by the built-in electric field at the heterojunction interface.[19–24] To realize broadband detection, one feasible way is to find narrow bandgap materials,[25–28] which have the ability to absorb light with a wide spectrum. $AgIn_5Se_8$ (AIS), an n-type ternary semiconductor,[29] has a direct bandgap of 1.25 eV,[30] which enables photons to be excited from the valence band to the conduction band without the assistance of phonons.[31–35] Furthermore, AIS shows a high absorption coefficient, high optical conductivity and excellent light stability, which indicates that AIS demonstrates photodetection performance.[36–38] In our previous study, a $AgIn_5Se_8$/$FePSe_3$ heterojunction photodetector exhibited a fast photoresponse under broad spectral irradiation from 365 nm to 1020 nm.[36] However, the rough surface and the uncontrollable thickness of the $FePSe_3$ film resulted in poor quality of the heterojunction interfaces, which resulted in low responsivity and detectivity.

Selenide (Se), a p-type semiconductor, possesses a bandgap of about 1.7 eV with high electron mobility ($\sim 0.14\ cm^2 \cdot V^{-1} \cdot s^{-1}$) and high carrier concentration ($\sim 9.35 \times 10^{16}\ cm^{-3}$), and also shows significant conductivity change upon illumination.[39–45] Furthermore, due to chain-like molecules, Se tends to form low-dimensional structures, such as microtubules, nanoribbons and nanowires, which can effectively increase the contact area of heterojunctions and further increase the photodetection performance.[46,47]

In this work, continuous and dense trigonal-Se (t-Se) films were prepared by electrochemical deposition[48] and the AIS/t-Se heterojunction was further fabricated. The AIS/t-Se photodetector based on the heterojunction shows good self-powered broadband photodetection and fast photoresponse performance at $V_{bias} = 0$ V. Compared with AIS/FPS heterojunction photodetectors,[36] the R and D^* values of the AIS/t-Se heterojunction photodetectors increased 9 and 4 times, respectively. The better performance is mainly due to the formation of the t-Se nanoribbons and the further increased contact area of the heterojunction interface, which optimized the

[†]Corresponding author. E-mail: hupeng@nwu.edu.cn

© 2023 Chinese Physical Society and IOP Publishing Ltd

carriers' transport path and increased the self-powered photoresponse. The results indicate that the AIS/t-Se heterojunction photodetector is a promising candidate for ultrafast, self-powered and broadband photodetection.

2. Experiment details

2.1. Material preparation

The preparation of AIS was carried out according to our previous work.[36] The t-Se films were grown *in situ* by electrochemical deposition[48] which was carried out in a three-electrode system. An ITO plate (1×2 cm^2), Pt sheet (1×1 cm^2) and Ag/AgCl were used as the working, counter and reference electrodes, respectively. A Na_2SeO_3 solution (0.01 mol/L) was used as the electrolyte. The pH and the temperature for deposition were 2 °C and 80 °C, respectively. The electrochemical deposition potential was determined to be −0.7 V by cyclic voltammetry (CV), as shown in Fig. S1.

2.2. Device fabrication

The t-Se film was immersed in DI water for 10 min to remove the Na_2SeO_3 on the surface, and 100 mg AIS flakes were dispersed in 500 μL DI water via 30 min ultrasonic treatment as an AIS precursor. Then, the dispersed AIS precursor was drop-cast on the t-Se film. The AIS/t-Se heterojunction photodetector was obtained after drying for 30 min at 60 °C under vacuum. Silver was spot-coated on the surface of the AIS film and ITO glass as the electrodes, and the effective illumination area of the heterojunction photodetector was 5.8×10^{-3} cm^2 (Fig. S2).

2.3. Characterization

The phases and morphology of the materials were analyzed using x-ray diffraction (XRD, DX-2700, Hao Yuan, China), scanning electron microscopy (SEM, FEI Apreo S) and high-resolution transmission electron microscopy (TEM, FEI Tecnai G2 F20). The elemental composition and atomic chemical states of the materials were analyzed using x-ray photoelectron spectroscopy (XPS, ESCALAB Xi$^+$). Diffuse reflectance spectra and the optical bandgap of the materials were obtained using a UV–Vis–NIR spectrophotometer (PerkinElmer Lambda 950). Steady-state photoelectrical properties were measured using a KEYSIGHT B2901A source instrument and light-emitting diode lamps of different wavelengths, and a DHC GCI-73 electronic timer and a DHC GCI 7103M-B shutter were used to control light-switching.

3. Results and discussion

3.1. Characterization of AIS/t-Se

The phase purity of AIS was characterized by XRD, as shown in Fig. 1(a). The strong diffraction peaks at 26.55°, 44.20°, 52.29°, 64.14°, 70.56° and 80.97° correspond to the (112), (204), (116), (008), (316) and (228) lattice planes,[36] respectively, and no other peaks were observed, which indicated that the sample has a pure tetragonal phase, according to the JCPDS #191149. The SEM image (Fig. 1(b)) shows that AIS has a multilayer stacked structure. The elemental energy dispersive x-ray (EDAX) mapping (Fig. 1(c)) analysis verifies the uniform distribution of Ag, In and Se in AIS. The TEM image (Fig. 1(d)) also exhibits the multilayer structure of the AIS flakes. The HRTEM image (Fig. 1(e)) shows the crystal lattice spacing of 0.331 nm, corresponding to the (112) plane of tetragonal AIS crystals.

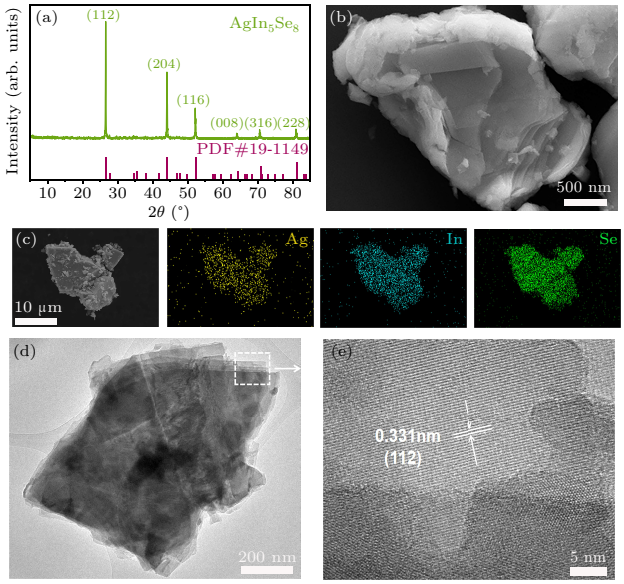


Fig. 1. (a) The XRD pattern of AIS. (b) The SEM image of AIS. (c) SEM-EDAX element mapping images for Ag, In, and Se. (d) The TEM image of AIS flakes. (e) The HRTEM image with lattice fringes of AIS flakes.

The t-Se films were prepared by electrochemical deposition. Figures 2(a)–2(c) show the SEM images of t-Se films obtained at an electrodeposition voltage of −0.7 V for 1.5 h, which exhibited a hemisphere morphology (Fig. 2(b)). With the deposition time increased, the edge and the center part of the t-Se hemisphere start to bulge and collapse (Fig. S3). Furthermore, more nanoribbons were formed to cover and connect the hemisphere (Fig. 2(b)). The thickness of the t-Se films was increased with the deposition time, which is 1.3 μm for the sample deposited for 1.5 h (Fig. 2(c)). The XRD results (Fig. 2(d)) indicated that the t-Se films had a pure phase with a preferable growth crystal plane of (011). The star (*) peaks around 30°–40° in Fig. 2(d) are attributed to ITO. The t-Se exhibits strong light absorption from 200 nm to 1200 nm (Fig. 2(e)). The optical bandgap can be calculated using the conventional Tauc equation

$$\alpha h\nu = A(h\nu - E_g)^{n/2}, \tag{1}$$

where α is the absorption coefficient, $h\nu$ is the photon energy, A is the constant, $n = 2$ for a directly allowed transi-

tion and $n = 4$ for an indirectly allowed transition. The $n = 2$ was used to calculate the optical bandgap of t-Se because it is a direct bandgap semiconductor.[49] The corresponding transformed reflectance spectra are shown in the inset of Fig. 2(e), where the intersection of the horizontal axis and the tangent line is the bandgap energy. Consequently, the calculated optical bandgap of t-Se is about 1.68 eV.

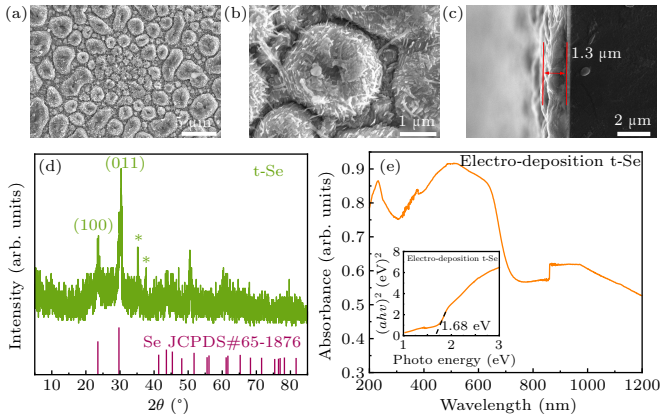


Fig. 2. (a)–(c) SEM images under the deposition voltage of −0.7 V. (d) The XRD pattern of AIS. (e) The optical diffuse reflectance absorption spectrum of t-Se. The inset shows the optical bandgap of t-Se.

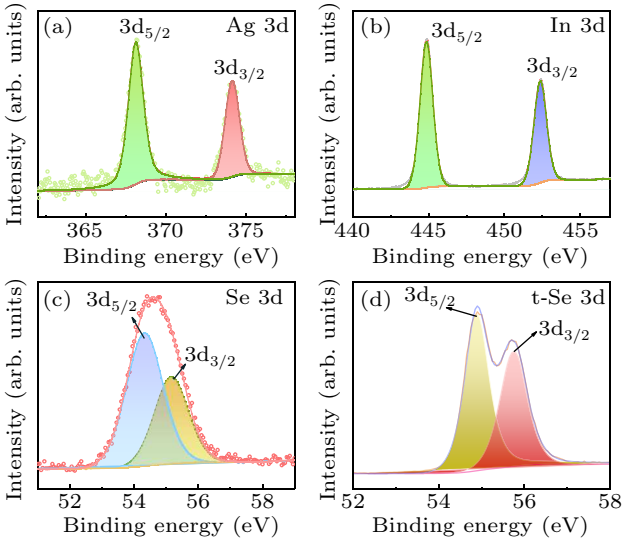


Fig. 3. High-resolution XPS spectra: (a) Ag 3d, (b) In 3d, and (c) Se 3d of AIS; (d) t-Se 3d.

The elementary composition and oxidation states of AIS and t-Se are identified by XPS. Two peaks are located at 374.1 eV and 368.1 eV, corresponding to Ag $3d_{3/2}$ and $3d_{5/2}$, respectively (Fig. 3(a)). In addition, the main peaks centered at 452.7 eV and 445.1 eV belong to $3d_{3/2}$ and $3d_{5/2}$ of In^{3+} (Fig. 3(b)), while two peaks at 55.2 eV and 54.1 eV can be assigned to Se $3d_{3/2}$ and Se $3d_{5/2}$ of Se^{2-} (Fig. 3(c)). Figure 3(d) shows the high-resolution XPS spectra of Se 3d in t-Se. The Se $3d_{5/2}$ and Se $3d_{3/2}$ are located at 54.8 eV and 55.7 eV, respectively, representing the t-Se. Due to the different valence states, the position of the peak is different from that of the Se 3d peak in AIS.[50,51]

3.2. Photodetection performances of photodetectors

A schematic diagram of the device structure of the AIS/t-Se heterojunction photodetector is shown in Fig. 4(a). The electrical and optical detection properties of the heterojunction devices were examined using a two-probe method under ambient conditions. The electrodeposition time dramatically affects the optoelectronic performance of the photodetector (Fig. S4). The device showed the largest photocurrent when the deposition time was 1.5 h at a deposition voltage of −0.7 V. The AIS/t-Se heterojunction photodetector exhibits a photocurrent of 80 nA at a bias voltage of −5 V under 780 nm illumination and a broadband photoresponse from 365 nm to 1200 nm (Fig. 4(b)). The short circuit current and open circuit voltage are 3.46 nA and −0.36 V, respectively, indicating the broadband self-powered characteristics of the devices (inset of Fig. 4(b)). The self-powered behavior of the AIS/t-Se heterojunction photodetector is mainly due to the separation of photocarriers by the built-in electric field of the heterojunction. The time-dependent photoresponse of the heterojunction device at different wavelengths at 0 V is shown in Fig. 4(c), which also indicates the broadband self-powered performance with the best photoresponse at 780 nm.

The single period time-resolved photocurrent on/off behavior (Fig. 4(d)) shows a clear on-state and off-state under light illumination and in the dark, respectively. The rise time (τ_r) and decay time (τ_d) are defined as the time difference between the photocurrent rising from 10% to 90% and falling from 90% to 10%, respectively. The rise time and decay time (τ_r/τ_d) of the AIS/t-Se devices are estimated to be 0.2 s and 0.04 s, respectively. The multi-period I–t curves (Fig. 4(e)) of the photodetector under 780 nm illumination indicate good stability and reproducibility with light switching. The I–t curves of the heterojunction photodetector under 780 nm illumination with different optical power densities at $V_{bias} = 0$ V are shown in Fig. 4(f). The photocurrent and the on/off ratio increase to 2 nA and 260 at an optical power density of 9.9 mW/cm^2. The relationship between the optical power density and the photocurrent is shown in Fig. 4(g), which can be fitted by the function of $I_{ph} = P^{\alpha}$. The parameter α is calculated to be 0.61, indicating the existence of defects and/or trap states inside the photodetector.

Responsivity (R) and detectivity (D^*) are two important parameters that are used to evaluate the performance of a photodetector, which can be calculated using the following equations:

$$R = \frac{I_{ph}}{P \times S}, \tag{2}$$

$$D^* = R\sqrt{\frac{S}{2eI_{dark}}}, \tag{3}$$

where I_{ph} is the photocurrent, P is the optical power density, S is the effective illumination area, and e is the fundamental

charge value. Figure 4(h) shows the R and D^* of the photodetector under different wavelengths of light at a bias voltage of 0 V. The dark current is 0.78×10^{-11} A and the photocurrent is 1.81×10^{-9} A, respectively. The device exhibited maximum R and D^* values of 32 μA/W and 1.8×10^9 Jones under 780 nm illumination, respectively, which showed an increment of about 9 and 4 times, respectively, compared with those of the AIS/$FePSe_3$ devices. The R and D^* are not only related to the photocurrent, but also to the optical power density. Therefore, the trends in the photocurrent with different wavelengths are different from the trends in the R and D^*. Detailed values of optical power densities at different wavelengths are shown in Table S1. Compared with other typical thin-film heterojunction self-powered photodetectors, the optoelectronic performances are comparable to or better than most of the previous results (Table S2), which could be useful in fast broadband photodetection. The performance improvement is attributed to the formation of the t-Se nanoribbons and the relatively smooth t-Se film at the interface. Thus, the contact area of the heterojunction interface is increased, which optimizes the carriers' transport path and increases the photoresponse.

As shown in Figs. 4(i) and S5, the performance of the heterojunction photodetector was tested by controlling the on/off speed of the optical switch at $V_{bias} = 0$ V with different frequencies of incident light. When the on/off speed is 10 s (0.1 Hz), 1 s (1 Hz) and 0.1 s (10 Hz), the device exhibits a significant photoresponse to 780 nm light. In addition, different frequencies of incident light affect the magnitude of the photocurrent. With different frequencies of 0.1 Hz, 1 Hz, and 10 Hz, our photodetector showed a fast switching response and good reproducibility. The photocurrent of the device decreased by only 6% at 1 Hz compared to 0.1 Hz, which is the result of recombination due to trap densities in AIS thin film.[52] The results indicated that the AIS/t-Se heterojunction photodetectors have the ability to detect flickering light signals.

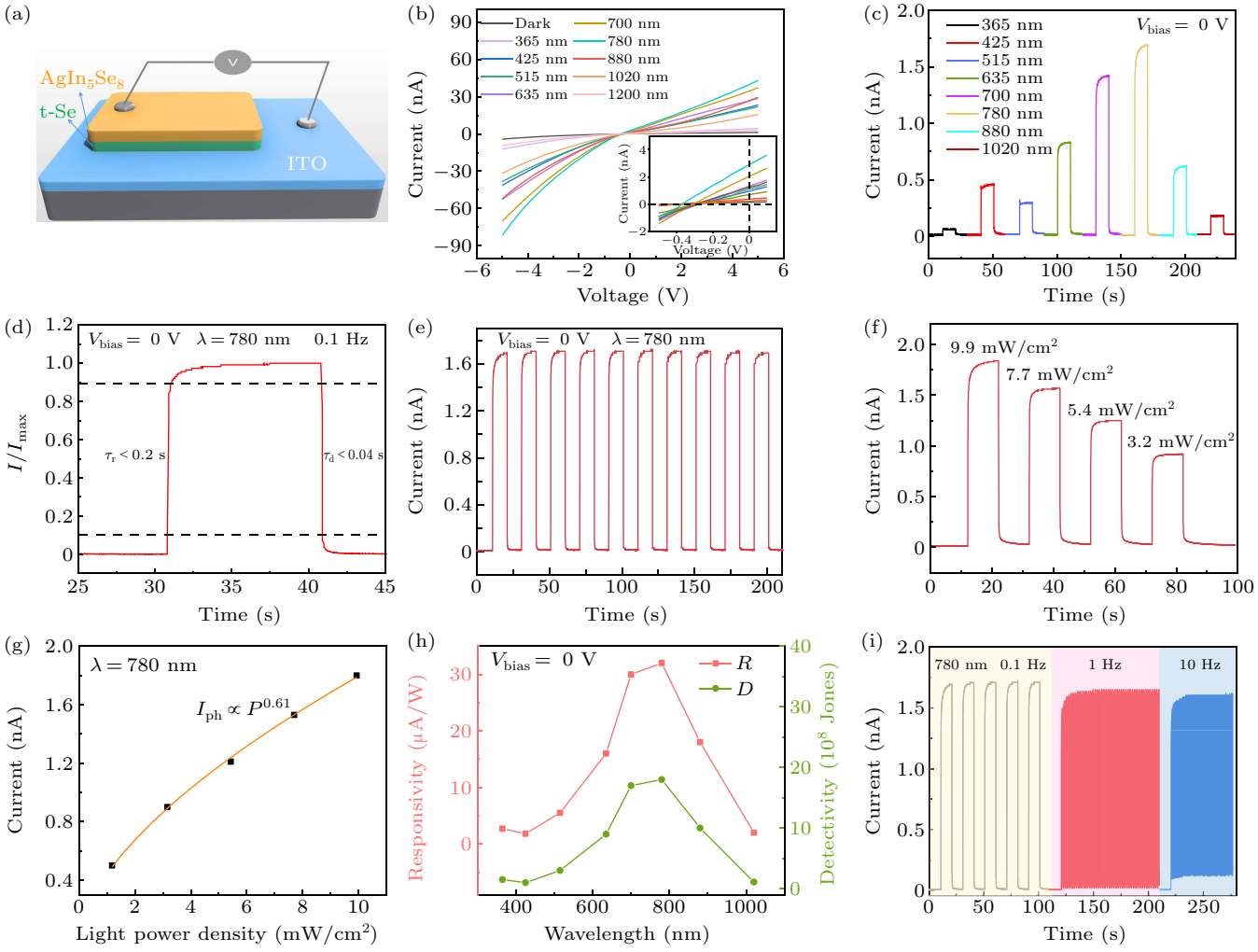


Fig. 4. The photoresponse performance of the photodetector. (a) The device structure of the AIS/t-Se heterojunction. (b) I–V curves of the device illuminated at different wavelengths. The inset is the magnified I–V curve. (c) I–t curves of different wavelengths at $V_{bias} = 0$ V. (d) The multi-period I–t curve of the device response to 780 nm light at zero bias voltage. (e) The single cycle curve at 780 nm light illumination. (f) I–t curves of the device at different optical power densities at 780 nm ($V_{bias} = 0$ V). (g) The relationship between different optical power densities and photocurrent at $V_{bias} = 0$ V. (h) The responsivity and detectivity of the AIS/t-Se heterojunction photodetector at different wavelengths ($V_{bias} = 0$ V). (i) I–t curves of the device at different incident light frequencies at 780 nm.

To understand the self-powered mechanism of the AIS/t-Se photodetector, the energy band diagram of the AIS/t-Se heterojunction is shown in Fig. 5. The work function, valence band position and the bandgap of AIS are 4.43 eV, 1.22 eV and 1.34 eV, respectively.[36] The work function of t-Se is 5.07 eV, determined by UPS measurements (Fig. S6(a)), and the valence band position is 0.28 eV (Fig. S6(b)), by XPS. The energy band arrangement of the AIS/t-Se heterojunction photodetector is obtained by considering the above values and the bandgap of t-Se. Since the Fermi energy level of AIS is higher than that of t-Se, the electrons drift from AIS to t-Se after contact until the Fermi energy level reaches the same level. At the same time, a built-in electric field is formed at the interface of the heterojunction with the direction from AIS to t-Se by the diffusion of carriers. When the energy of the light is larger than the bandgap of the AIS, the photogenerated electron–hole pairs separate rapidly due to the presence of the built-in electric field.[53] With the electrons moving toward the conduction band of the AIS and the holes moving toward the valence band of t-Se, a photovoltage is formed at the interface of the heterojunction, resulting in a self-powered optical response.

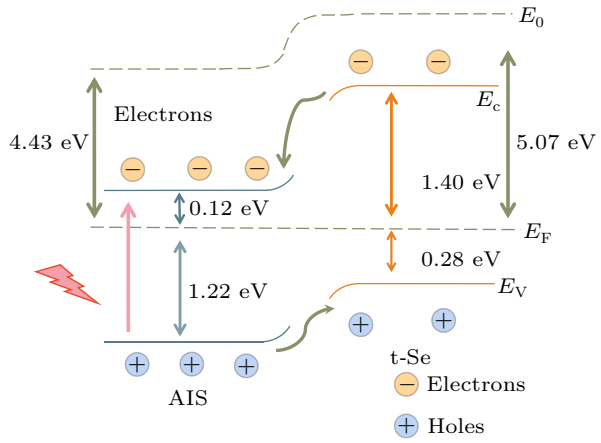


Fig. 5. Energy band diagram of the AIS/t-Se heterojunction photodetector.

4. Conclusion

In summary, continuous and dense t-Se thin films were prepared via an electrochemical deposition method using 0.01 mol/L Na_2SeO_3 solution as the electrolyte. When the electrochemical was deposited at −0.7 V for 1.5 hours, a large number of t-Se nanoribbons were formed, which resulted in the best photoelectrical performance of the AIS/t-Se heterojunction device. The AIS/t-Se photodetector demonstrates a self-powered performance under broad spectral irradiation from 365 nm to 1020 nm with the best R and D^* values of 32 μA/W and 1.8×10^9 Jones, respectively, under 780 nm at 0 V. This result indicates that the t-Se nanoribbons significantly enhance the performance of the heterojunction photodetector. The AIS/t-Se heterojunction device demonstrates better optoelectronic performance than the AIS/FPS heterojunction device, showing about 9 and 4 times increases in R and D^*, respectively. This work provides a potential approach to realize ultrafast and self-powered optoelectronic devices based on AIS.

Acknowledgments

Project supported by the National Natural Science Foundation of China (Grant No. 51803168), the Key Research and Development Program of Shaanxi Province (Grant No. 2022GY-356), and the Youth Innovation Team of Shaanxi Universities.

References

[1] Jack W J 2001 *Smart Mater. Struct.* **10** 1115
[2] Simone G, Di Carlo Rasi D, de Vries X, Heintges G H L, Meskers S C J, Janssen R A J and Gelinck G H 2018 *Adv. Mater.* **30** 1804678
[3] Wang Q, Zhang Y and Wei Z 2023 *Chin. J. Chem.* **41** 958
[4] Bao C, Yang J, Bai S, Xu W, Yan Z, Xu Q, Liu J, Zhang W and Gao F 2018 *Adv. Mater.* **30** 1803422
[5] Qiu Q and Huang Z 2021 *Adv. Mater.* **33** e2008126
[6] Long M, Wang P, Fang H and Hu W 2018 *Adv. Funct. Mater.* **29** 1803807
[7] Qiao H, Huang Z, Ren X, Liu S, Zhang Y, Qi X and Zhang H 2019 *Adv. Opt. Mater.* **8** 1900765
[8] Wang H and Kim D H 2017 *Chem. Soc. Rev.* **46** 5204
[9] Jin Z, Hu C, Lan Y, Cao Y, Deng H, Yang X, Wang J and Song H 2020 *Adv. Opt. Mater.* **8** 2001319
[10] Wang C, Zhang X and Hu W 2020 *Chem. Soc. Rev.* **49** 653
[11] Fang H, Zheng C, Wu L, Li Y, Cai J, Hu M, Fang X, Ma R, Wang Q and Wang H 2019 *Adv. Funct. Mater.* **29** 1809013
[12] Jokar E, Cai L, Han J, Nacpil E J C and Jeon I 2023 *Chem. Mater.* **35** 3404
[13] Xu H, Liu J, Zhang J, Zhou G, Luo N and Zhao N 2017 *Adv. Mater.* **29** 1700975
[14] Cho Y, Jung H R and Jo W 2022 *Nanoscale* **14** 9248
[15] Wang W, Zhao D, Zhang F, Li L, Du M, Wang C, Yu Y, Huang Q, Zhang M, Li L, Miao J, Lou Z, Shen G, Fang Y and Yan Y 2017 *Adv. Funct. Mater.* **27** 1703953
[16] Dang Z, Wang W, Chen J, Walker E S, Bank S R, Akinwande D, Ni Z and Tao L 2021 *2D Mater.* **8** 035002
[17] Wu S, Chen Y, Wang X, Jiao H, Zhao Q, Huang X, Tai X, Zhou Y, Chen H, Wang X, Huang S, Yan H, Lin T, Shen H, Hu W, Meng X, Chu J and Wang J 2022 *Nat. Commun.* **13** 3198
[18] Yu P, Hu K, Chen H, Zheng L and Fang X 2017 *Adv. Funct. Mater.* **27** 1703166
[19] Zhu T, Su J, Alvarez J, Lefèvre G, Labat F, Ciofini I and Pauporté T 2019 *Adv. Funct. Mater.* **29** 1903981
[20] Shen T L, Chu Y W, Liao Y K, Lee W Y, Kuo H C, Lin T Y and Chen Y F 2020 *Adv. Opt. Mater.* **8** 1901334
[21] Chen H, Yu P, Zhang Z, Teng F, Zheng L, Hu K and Fang X 2016 *Small* **12** 5809
[22] Yang D, Du F, Ren Y, Kang T, Hu P, Teng F and Fan H 2021 *J. Mater. Chem. C* **9** 14146
[23] Jiao H, Wang X, Wu S, Chen Y, Chu J and Wang J 2023 *Appl. Phys. Rev.* **10** 011310
[24] Zhou X, Li N and Lu W 2019 *Chin. Phys. B* **28** 027801
[25] Jenekhe S A 1986 *Nature* **322** 345
[26] Wu L and Yang Y 2022 *Adv. Mater. Interfaces* **9** 2201415
[27] Wu Y, Qiu L, Liu J, Guan M, Dai Z and Li G 2022 *Adv. Opt. Mater.* **10** 2102661
[28] Yu X, Li Y, Hu X, Zhang D, Tao Y, Liu Z, He Y, Haque M A, Liu Z, Wu T and Wang Q J 2018 *Nat. Commun.* **9** 4299
[29] Shen X, Wang G, Li S, Yang C C, Tan H, Zhang Y, Lu X, He J, Wang G and Zhou X 2019 *J. Alloys Compds.* **805** 444
[30] Song S, Liang Z, Fu W and Peng T 2017 *ACS Appl. Mater. Interfaces* **9** 17013
[31] Begum Y, Khan S, Reshak A H, Laref A, Amir Z, Murtaza G, Bila J, Johan M R and Al-Noor T H 2021 *Int. J. Energy Res.* **45** 4014
[32] Qasrawi A F 2008 *J. Alloys Compd.* **455** 295

[33] Matsumoto R, Hou Z, Hara H, Adachi S, Tanaka H, Yamamoto S, Saito Y, Takeya H, Irifune T, Terakura K and Takano Y 2020 *Inorg. Chem.* **59** 325

[34] Makhova L V, Konovalov I and Szargan R 2004 *Phys. Status Solidi A* **201** 308

[35] Gasanly N M 2016 *Infrared Phys. Technol.* **75** 168

[36] Lu Q, Xu L, Ren Y, Gao J, Chen Y, Song J, Fan H, Teng F, He X and Hu P 2022 *ACS Appl. Electron. Mater.* **4** 5284

[37] Benoit P, Djega-Mariadassou C, Lesueur R and Albany J H 1979 *Phys. Lett. A* **73** 55

[38] Shen X, Zhang B, Chen Q, Tan H, Zhang X, Wang G, Lu X and Zhou X 2019 *Inorg. Chem. Front.* **6** 3545

[39] Liang J W, Firdaus Y, Kang C H, Min J W, Min J H, Al Ibrahim R H, Wehbe N, Hedhili M N, Kaltsas D, Tsetseris L, Lopatin S, Zheng S, Ng T K, Anthopoulos T D and Ooi B S 2022 *ACS Appl. Mater. Interfaces* **14** 17889

[40] Luo L B, Yang X B, Liang F X, Jie J S, Li Q, Zhu Z F, Wu C Y, Yu Y Q and Wang L 2012 *CrystEngComm* **14** 1942

[41] Gates B, Mayers B, Cattle B and Xia Y 2002 *Adv. Funct. Mater.* **12** 219

[42] Chang Y, Huang L, Zhou Y, Wang J and Zhai W 2022 *ACS Appl. Mater. Interfaces* **14** 5624

[43] Bube R H 1955 *Proc. Inst. Radio Eng.* **43** 1836

[44] Hu K, Chen H, Jiang M, Teng F, Zheng L and Fang X 2016 *Adv. Funct. Mater.* **26** 6641

[45] Liu P, Ma Y, Cai W, Wang Z, Wang J, Qi L and Chen D 2007 *Nanotechnology* **18** 205704

[46] Wang Y, Zhang A, Shao Z, Yu H, Xu Y, Liu X, Cui M, Gao F, Hu P and Feng W 2022 *Adv. Opt. Mater.* **10** 2201926

[47] Hu K, Teng F, Zheng L, Yu P, Zhang Z, Chen H and Fang X 2017 *Laser Photonics Rev.* **11** 1600257

[48] Seyedmahmoudbaraghani S, Yu S, Lim J and Myung N V 2020 *Front. Chem.* **8** 785

[49] Chang Y, Zhou Y, Wang J and Zhai W 2022 *Small* **18** e2201714

[50] Huang H, Ma C, Zhu Z, Yao X, Liu Y, Liu Z, Li C and Yan Y 2018 *Chem. Eng. J.* **338** 218

[51] Zhang J, Fu Q, Xue Y and Cui Z 2018 *CrystEngComm* **20** 1220

[52] Zeng L H, Wu D, Lin S H, Xie C, Yuan H Y, Lu W, Lau S P, Chai Y, Luo L B, Li Z J and Tsang Y H 2019 *Adv. Funct. Mater.* **29** 1806878

[53] Cao B, Liu Q, Zheng Y, Tang X, Chai J, Ma S, Wang W and Li G 2022 *Adv. Funct. Mater.* **32** 2110715